THE JOURNAL OF PHYSICAL CHEMISTRY C
Article
pubs.acs.org/JPCC

Redox Processes of Manganese Oxide in Catalyzing Oxygen Evolution and Reduction: An *in Situ* Soft X-ray Absorption Spectroscopy Study

Marcel Risch,*[,†] Kelsey A. Stoerzinger,[‡] Binghong Han,[‡] Tom Z. Regier,[∥] Derek Peak,[⊥] Sayed Youssef Sayed,[†] Chao Wei,[#] Zhichuan Xu,[#] and Yang Shao-Horn*[,†,‡,§]

[†]Research Laboratory of Electronics, [‡]Department of Materials Science and Engineering, and [§]Department of Mechanical Engineering, Massachusetts Institute of Technology, Cambridge, Massachusetts 02139, United States

[∥]Canadian Light Source, Inc., Saskatoon, Saskatchewan S7N 2 V3, Canada

[⊥]Department of Soil Science, University of Saskatchewan, Saskatoon, Saskatchewan S7N 5A8, Canada

[#]School of Materials Science and Engineering, Nanyang Technological University, 639798 Singapore

Supporting Information

ABSTRACT: Manganese oxides with rich redox chemistry have been widely used in (electro)catalysis in applications of energy and environmental consequence. While they are ubiquitous in catalyzing the oxygen evolution reaction (OER) and oxygen reduction reaction (ORR), redox processes occurring on the surface of manganese oxides are poorly understood. We report valence changes at OER- and ORR-relevant voltages of a layered manganese oxide film prepared by electrodeposition. X-ray absorption spectra were collected *in situ* in O_2-saturated 0.1 M KOH using inverse partial fluorescence yield (IPFY) at the Mn $L_{3,2}$-edges and partial fluorescence yield (PFY) at the O K-edge. Overall, we found reversible yet hysteretic Mn redox and qualitatively reproducible spectral changes by Mn $L_{3,2}$ IPFY XAS. Oxidation to a mixed $Mn^{3+/4+}$ valence preceded the oxygen evolution at 1.65 V vs RHE, while manganese reduced below Mn^{3+} and contained tetrahedral Mn^{2+} during oxygen reduction at 0.5 V vs RHE. Analysis of the pre-edge in O K-edge XAS provided the Mn−O hybridization, which was highest for Mn^{3+} (e_g^1). Our study demonstrates that combined *in situ* experiments at the metal L- and oxygen K-edges are indispensable to identify both the active valence during catalysis and the hybridization with oxygen adsorbates, critical to the rational design of active catalysts for oxygen electrocatalysis.

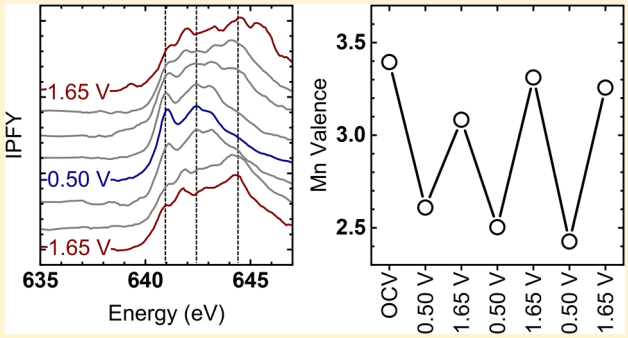

INTRODUCTION

Manganese oxides have rich redox chemistry and are thus a prime choice for energy storage and conversion both in nature and industrial applications. In nature, oxygen evolution is performed by a $CaMn_4O_5$ cluster in photosystem II (PSII),[1,2] which has inspired much research in homogeneous and heterogeneous (photo)electrocatalysis of the oxygen evolution reaction (OER).[2−9] The $CaMn_4O_5$ motif can also be found in several layered oxides,[10−14] among which are layered birnessites (δ-$A_xMnO_{2-y}\cdot zH_2O$, A = Na, K, Ca, and Sr).[10−13,15−18] In addition, Mn oxides with perovskite,[19,20] bixbyite,[21] and spinel[22] structures can exhibit reasonable activity in catalyzing OER. Moreover, Mn oxides are among the most active for the oxygen reduction reaction (ORR),[23−26] where the ones with perovskite,[27] bixbyite,[28] and spinel[22,23,29,30] structures show high ORR activity. Due to suitable kinetics for both OER and ORR, Mn oxides are studied as bifunctional electrocatalysts in metal−air batteries.[31−33] Furthermore, their redox chemistry makes Mn oxides promising candidates for charge storage in electrochemical capacitors[34−36] and batteries[37−39]

Mn oxides form layered, spinel, perovskite, and bixbyite structures, where Mn ions can have a wide range of valence states usually from 2+ to 4+,[10,12,16,18,20−22,31,40−52] exhibiting different catalytic activities for OER and ORR kinetics.[21,23,45,53] A number of studies have employed *ex situ* methods to correlate Mn valence with OER and ORR activity, using either X-ray absorption spectroscopy (XAS) at the Mn K-edge (hard XAS)[10,15,22,40−42,54,55] to probe unoccupied Mn-4p orbitals or the Mn $L_{3,2}$-edges (soft XAS)[43−46] to probe unoccupied Mn-3d orbitals or by using X-ray photoelectron spectroscopy (XPS)[16,20,21,31,41,43] to probe binding energies of occupied states (e.g., of Mn 2p electrons). However, ambiguities exist in

Received: June 7, 2017
Revised: July 23, 2017
Published: July 23, 2017

DOI: 10.1021/acs.jpcc.7b05592
J. Phys. Chem. C 2017, 121, 17682−17692

what Mn valence is responsible for OER or ORR activity among the *ex situ* studies in literature.

Electrodeposited and subsequently crystallized films of $Mn^{3+}{}_2O_3$ (with minor Mn^{2+} impurities) show OER activity in 1.0 M KOH higher than those containing more Mn^{2+} or Mn^{4+} from *ex situ* XPS work.[21] This study detects little Mn^{4+} after the oxidizing conditions of the OER.[21] Moreover, a recent study by Wei et al.[22] shows increasing activity of $MnCo_2O_4$ in 0.1 M KOH with reduction from $Mn^{3.7+}$ to $Mn^{3.2+}$ based on *ex situ* K-edge XAS. The highest OER activity (1.52 V vs RHE at 25 $\mu A/cm^2{}_{ox}$) is observed for Mn_3O_4,[22] where it is argued that octahedral Mn^{3+} is the active site. However, an optimal Mn valence in the range of $Mn^{3.6+}$ to $Mn^{3.8+}$ for the OER on various Mn oxides in 0.1 M KPi by *ex situ* XPS[16] and *ex situ* K-edge XAS[10,15] studies, where the catalyst is composed exclusively of Mn octahedra. Higher valences approaching Mn^{4+} have also been detected for these materials after the OER in both 0.1 M KOH and KPi by *ex situ* K-edge XAS.[14] On the basis of *ex situ* L-edge XAS, Gorlin et al.[43] find that the extent of valence changes after OER in 0.1 M KOH depends on the crystallinity that can be greatly influenced by the heat treatment in the preparation of the catalyst.

With regard to ORR kinetics, Mn perovskites with mixed valence of Mn^{3+} and Mn^{4+} have intrinsic activities in 0.1 M KOH of up to 1.3 $mA/cm^2{}_{ox}$ at 0.8 V vs RHE,[23,27] which is higher than those containing exclusively Mn^{4+} as measured by *ex situ* L-edge[46] and K-edge[22,41] XAS, which suggests that having Mn^{3+} is critical to obtain high activity.[46] In addition, spinels containing Mn^{3+} and Mn^{2+} also exhibit high activities of up to 0.7 $mA/cm^2{}_{ox}$ at 0.8 V vs RHE for the ORR in 0.1 M KOH,[23,29,30] corroborating that Mn^{3+} is essential to catalyze the ORR. It has recently been shown that the e_g occupation of the octahedral site in these spinels is the activity descriptor for ORR,[22] which shows the maximum activity (0.88 V vs RHE at 25 $\mu A/cm^2{}_{ox}$) for $Mn^{3.4+}$. This is the same Mn valence as reported for the most active perovskite oxide in the $La_{1-x}Sr_xMnO_3$ series.[23] Thus, these observations are in agreement with the hypothesis that having a mixed Mn valence between Mn^{3+} and Mn^{4+} can improve the charge transfer to adsorbed oxygen and therefore improve the ORR activity.[23]

The dynamic range of accessible Mn valence states near the potentials of oxygen evolution and reduction (O_2/OH^-) suggests the valence may change during these electrocatalytic processes, which calls for detection and correlation of potential-dependent Mn valence by *in situ* characterization. Such studies have been performed using hard X-rays at the Mn K-edge.[12,18,42,47−50,55,56] Mn valence changes can also be tracked using UV−vis spectroscopy after suitable calibration with another method.[12,15,55,57,58] Zaharieva et al.[12] report an oxidation of up to 0.5 Mn valence states before the onset of OER in an *in situ* experiment in 0.1 M KPi, where Mn^{3+} at catalytic voltages is proposed as a prerequisite for OER activity in electrodeposited layered Mn oxides. Similar observations are noted by Gorlin et al.,[18] where oxidation of electrodeposited Mn oxide films during the OER at 1.8 V vs RHE in 0.1 M KOH result in a mixed $Mn^{3+/4+}$ oxide with layered structure. Oxidation of electrodeposited[51,59,60] and photodeposited[50] Mn oxide prior to the OER is also reported in near-neutral solutions of 0.1 M KPi by Mn $L_{3,2}$-edge XAS,[51,60] 0.1 M Na_2SO_4 by Mn K-edge XAS,[50] and 2 M KCl by Mn K-edge XAS.[59] Addition of Au to the electrode increases the Mn valence of reactively sputtered Mn_3O_4 films as compared to identical potentials on Au-free electrodes.[49]

With regard to ORR, *in situ* Mn K-edge work of Lima et al.[47] reveals the reduction of β-MnO_2 and the formation of Mn_3O_4 (with tetrahedral Mn^{2+} and octahedral Mn^{3+}) at 0.70 V vs RHE in 1.0 M KOH, which is in agreement with the work of Gorlin et al.[18] finding the formation of Mn_3O_4 from electrodeposited Mn oxide during ORR at 0.7 V vs RHE in 0.1 M KOH. At higher ORR overpotentials (~0.3 V vs RHE), significant fractions of octahedral Mn^{2+} are observed (e.g., in the $Mn(OH)_2$ phase).[47,48] Since only the valence of the octahedral sites was proposed to trend with activity,[22] it is crucial to track both the oxygen coordination and valence of the active Mn cations during *in situ* experiments.

Extracting coordination and valence from soft XAS has several advantages over hard XAS. While hard XAS at the Mn K-edge probes Mn 4p orbitals,[61] soft XAS at the Mn $L_{3,2}$-edges is ideally suited to elucidate the Mn valence and coordination symmetry because Mn 3d orbitals are probed directly.[62] The core hole broadening at the Mn K-edge is 1.2 eV, while it is only 0.3 eV at the Mn L_3-edge.[63] This allows resolution of more fine structure at the Mn L_3-edge so that Mn valence and coordination in mixed valence oxides can be better distinguished. It also makes *in situ* studies at the Mn $L_{3,2}$-edges an attractive alternative to time-consuming analysis required for extended X-ray absorption fine structure (EXAFS) studies. Furthermore, this information is contained in an energy range of 10 eV at the Mn L_3-edge, while an energy range of about 550−975 eV (k_{max} = 12−16 $Å^{-1}$) is commonly recorded for EXAFS.[64] Thus, higher time resolution is achievable by *in situ* experiments at the Mn L_3-edge due to the shorter energy range and therefore acquisition time. In addition, the approximate attenuation lengths of the X-rays are a factor 100 shorter at the Mn L_3-edge (~100 nm) as compared to the Mn K-edge (~10 μm).[65] The attenuation length at the Mn L_3-edge is thus better matched with typical thicknesses of electrodeposited films for *in situ* XAS of 100 nm[18] or less.[66] Unfortunately, there are very few demonstrations of Mn valence changes at the Mn $L_{3,2}$-edges[51,60] due to the enormous challenges associated with *in situ* XAS of Mn at these low energies. These X-ray transmission studies demonstrated oxidation and subsequent reduction of an electrodeposited Mn oxide during a single voltage cycle[51] and Mn reduction during potentiostatic activation.[60] The soft XAS regime also gives access to analysis of the O K-edge, which provides valuable complementary insight into the electronic structure but has never before been performed *in situ* for Mn oxides and is rarely performed for other transition metal oxides.[42,67−69]

In this study, we report valence changes of an electrodeposited Mn oxide film in O_2-saturated 0.1 M KOH *in situ* as a function of voltage, extending from ORR to OER regions for multiple cycles. Mn $L_{3,2}$ spectra of the electrodeposited film provide high sensitivity to valence changes of Mn ions when detected using the inverse partial fluorescence yield (IPFY).[70] Using Mn $L_{3,2}$ IPFY XAS, we found overall reversible yet hysteretic Mn redox in a single cycle and qualitatively reproducible spectral changes during repeated voltage cycling. Lastly, the Mn−O hybridization was studied *in situ* by O K-partial fluorescence yield (PFY) XAS. Combining Mn $L_{3,2}$ and O K-edge analysis yielded a more comprehensive picture of dynamic changes of both Mn valence and Mn−O hybridization as a function of potential, which is critical to gain insights into the active sites catalyzing ORR and OER.

DOI: 10.1021/acs.jpcc.7b05592
J. Phys. Chem. C 2017, 121, 17682−17692

EXPERIMENTAL SECTION

Materials. The following Mn oxides were obtained commercially as references: MnO (99.99%, Alfa Aesar), Mn_3O_4 (97%, Sigma-Aldrich), β-MnO_2 (99.999%, Alfa Aesar), and $KMnO_4$ (99%, Sigma-Aldrich). Additionally, δ-$K_xMnO_{2-y}\cdot zH_2O$ was synthesized by reacting $MnSO_4$ with $KMnO_4$ in aqueous solution.[71] Transmission electron microscopy electron diffraction of reference δ-$K_xMnO_{2-y}\cdot zH_2O$ powder revealed a hexagonal layered structure (space group $P6_3/mmc$; Figure S1). Further details about the references may be found in Table S1.

The electrodeposited films were prepared following the work of Nakayama et al.,[72] where a potential of 1.33 V vs RHE was applied for a controlled charge of 10.3 mC/cm^2 (inset of Figure S2). All areas in this work refer to the geometric surface area of the electrode that was accessible to the electrolyte. Electrolytes for electrodeposition were prepared by adding 50 mM KCl (99% Sigma-Aldrich) and 2 mM $KMnO_4$ (99% Sigma-Aldrich) to deionized water (>18 MΩ cm), which had a pH of 6.5 at room temperature. Complete removal of $KMnO_4$ from electrodeposition was confirmed by recording a Mn $L_{3,2}$-edge spectrum in an XAS cell filled with water (Figure S3), which exhibited no characteristic peaks of $KMnO_4$. While the crystal structures of these electrodeposited thin films were difficult to resolve by X-ray diffraction, thicker films made by the same protocol can be assigned to the birnessite structure.[72]

XAS Cell. The three-electrode XAS cell used was developed based on a previously used flow cell.[73] It was made from Durus Black[73] with a leak-free silver chloride reference electrode (Harvard Apparatus) and a Pt counter electrode (Figure S4A). The XAS window was a commercial 20 nm Au on a 100 nm silicon nitride membrane with a 5 nm Cr binding layer (Norcada Inc. NX5100C).

Electrochemical Measurements. Electrolytes of 0.1 M KOH were prepared using deionized water (>18 MΩ cm) and KOH pellets with 99.98% purity (Alfa Aesar; at MIT) or 88.15% purity (Fisher Scientific; at the beamline). For activity measurements, oxygen (99.994% purity, Airgas) was bubbled to ensure O_2/HO^- equilibrium at 1.23 V vs RHE, while argon (99.999% purity, Airgas) was bubbled prior to background measurements for at least 30 min. Electrochemical characterization at the beamline was performed using a Voltalab PGZ-301 potentiostat. The reference electrode was calibrated in a laboratory glass cell using Pt working and counter electrodes in 0.1 M H_2-saturated KOH where the average voltage at zero current was taken as the reference voltage (1.006 V). The electrolyte was drawn through the flow cell using a Palmer syringe pump at a rate of 50 μL/min (500 μL/min for last 1.65 V step in cycle 3 due to O_2 buildup).

The electrodeposited δ-$K_xMn^{3.4+}O_{2-y}\cdot zH_2O$ on Au|CrO_x|Si_3N_4 was electrochemically characterized in the three-electrode XAS cell, where we found the expected features in a cyclic voltammogram in O_2-saturated 0.1 M KOH (Figure S4B, step 6 in Table S2). The redox peaks centered at ∼0.8 V vs RHE were previously observed for electrodeposited α-Mn_2O_3,[74] mixed MnO/MnO_2,[18] and β-$Mn^{IV}O_2$[47] particles in both N_2- and O_2-saturated 0.1 M KOH. During potentiostatic measurements, the currents at 0.50 V vs RHE were consistently negative owing to ORR while the currents at 1.65 V vs RHE were consistently positive owing to OER (Figure S4C). Currents collected at 1.20 and 1.50 V vs RHE had negative currents, which were not expected since the potentials were higher than the OCV of 1.07 V, indicating potential parasitic currents in the XAS cell. We can exclude pH changes in 0.1 M KOH for the observed currents (Figure S4C) due to high buffering capacity of water under these conditions (Supporting calculations).

X-ray Absorption Spectroscopy. X-ray absorption measurements at both the Mn $L_{3,2}$-edges and O K-edges were performed at the spherical grating monochromator (SGM) beamline 11ID-1 at the Canadian Light Source.[75] The window of the sample cells was mounted at an angle of roughly 45° with respect to both the incident beam and the detectors. The irradiated area on the cell window was about 0.05 mm^2, as estimated previously.[73] All measurements were conducted at room temperature in the fluorescence mode using Amptek silicon drift detectors (SDDs) with 1024 emission channels (energy resolution ≈ 120 eV). Four SDDs were employed simultaneously with vanadium (200 nm) filter foils mounted to suppress oxygen fluorescence. Gaussian curves were fitted to the oxygen and Mn emission lines of all SDDs at each incident energy where only the amplitude was varied freely. The incident intensity was obtained by measuring the current on a gold grid placed before the sample chamber.

PFY was then obtained from the Mn amplitude for Mn PFY in the range 632−676 eV and from the oxygen amplitude for oxygen PFY in the range 518−586 eV. Regardless of the range, the Mn L_3-edge intensity was reduced for Mn oxide powders due to self-absorption (Figure S5A). This makes it extremely challenging to distinguish fine details of the spectra around 640 eV. The IPFY was obtained from the inverse of the oxygen amplitude in the range 632−676 eV. In this range, the IPFY was free of self-absorption (Figure S5B) because the inverse of the nonresonant oxygen absorption is effectively a measure of the X-ray attenuation length.[70] Noting that there is no suitable Mn edge at energies lower than the O K-edge, we report the conventional PFY for the O K-edge. Oxygen PFY spectra were normalized for background absorption by fitting a straight line between 522 and 528 eV and subtracting it over the whole range of the data. Finally, the average intensity between 557 and 590 eV (after the O K-edge) was normalized to unity. The background of the *in situ* IPFY spectra was more complex due to the variation of the oxygen content (e.g., by electrochemical oxygen evolution). It required fitting an exponential function to the points of the local minimum between the L_3- and L_2-edge (around 650 eV) and after the L_2-edge (660−676 eV), which was then subtracted over the whole range of data. This was followed by the conventional subtraction of a constant before the L_3-edge and division of the average intensity around 650 eV (after Mn L_3-edge). For consistency, the same normalization was applied to powder references.

The energy axes of both O K- and Mn $L_{3,2}$-spectra were calibrated with respect to the pre-edge in the spectrum of molecular oxygen at 530.8 eV,[76] which was acquired by subtracting the spectrum of a pristine window in an oxygen atmosphere from that of a pristine window in an argon atmosphere (Figure S6). This differential approach was necessary because the pristine window contained a thin layer of chromium oxide to bind gold and silicon nitride. We use molecular oxygen as a reference for energy calibration because its purity is easier to ensure than that of metals which spontaneously form surface oxides. Moreover, evaluation is straightforward due to the very sharp prepeak of a molecular transition that can be calculated from first principles.[76] The energy positions of key spectral features of common oxides (suppliers in Table S1) with this energy calibration are

DOI: 10.1021/acs.jpcc.7b05592
J. Phys. Chem. C 2017, 121, 17682−17692

presented in Table S3 for the Mn L_3-edge and in Table S4 for the O K-pre-edge. These common oxides could be used for energy calibration and thus allow comparison with the work presented herein. The peak positions on our scale differ from those reported previously (Table S5), which does not affect the calculation of the Mn valence that relies on relative energies.

All experiments were performed at a flux of $\sim 7 \times 10^9$ photons/s, for which there were no indications of radiation damage in potassium permanganate (or all other Mn oxides; Figure S5), which is known for facile photoreduction.[77] Moreover, we found no indications of radiation damage at this dose in subsequent scans during the *in situ* experiment where the electrolyte was flown at 50 μL min^{-1} (Figure S7). At this rate, the sample volume in the cell of ~ 10 μL is completely replaced every 12 s. The sequence of all XAS measurements may be found in Table S2.

Linear Combination Analysis of the Mn $L_{3,2}$-edges. XANES fitting results depend critically on intensity normalization. To remove the effect of sample density variations and oxygen concentration, the Mn L-edge spectra were normalized to the average between 640 and 644 eV (Figure S8). Then, the rising part of the Mn L_3-edges was fit between 633.7 and 644.7 eV using Athena,[78] where a nonlinear least-squares procedure based on the Levenberg−Marquardt algorithm is employed. The XAS samples were fit using the spectra of $Mn^{2.7+}{}_3O_4$ and δ-$K_xMn^{3.4+}O_{2-y}{\cdot}zH_2O$ powders as standards with the constraints that the weights of each standard is between 0 and 1 and the two weights sum to 1. Other standards, particularly MnO_2 polytypes, were tested but discarded due to worse fits. While δ-$K_xMn^{3.4+}O_{2-y}{\cdot}zH_2O$ matched the oxidized state of the electrodeposited film very well (e.g., Figure S8A), Mn_3O_4 differed slightly from the reduced state of the electrodeposited film (e.g., Figure S8G). Thus, the necessity of additional standards cannot be rigorously excluded. However, the spectrum of Mn_3O_4 was the best match among Mn oxides with low oxidation state. State-dependent decay effects[79−81] might cause fluorescence yield measurements to deviate from true absorption cross sections of the Mn_3O_4 and δ-$K_xMn^{3.4+}O_{2-y}{\cdot}zH_2O$ phases. Fit uncertainties were obtained from the diagonal elements of the covariance matrix scaled by the square root of reduced chi-square ($1\sigma-$ uncertainty).

Fitting and Integration of the O K-Pre-Edge Region. O K-edge spectra were fit by Gaussian curves using the "multiple peak fit" tool in Origin 9.1. For the analysis of the Mn−O hybridization of the reference samples (Figure S9), we simultaneously fit Gaussian curves to a shoulder and the main O K-edge between 536.2 and 547.4 eV as a background, except for MnO, where an additionally fitted peak at ~530 eV was included in the background. The Gaussian curves were not offset ($y_0 = 0$). We also attempted to fit the pre-edge region, but the fits did not converge for some of the reference materials. We thus used a more robust integration approach. Experimental uncertainties were obtained by performing the analysis on individual scans and calculation of the standard deviation of the values.

For the *in situ* measurements of the electrodeposited film, we simultaneously fit three Gaussians between 520.0 and 535.5 eV (Figures S10 and S11). Two of these peaks constitute the pre-edge, while the shoulder in the O K-edge was also included as a background to the pre-edge. The range from 530.5 to 531.5 eV was excluded because an additional peak may emerge in this range. The widths of the peak centered at ~530 and ~523 eV were fixed to 1.8 and 1.4 eV. The position of the peak in the O K-edge was fixed to 533.0 eV. The Gaussian curves were not offset ($y_0 = 0$). All other parameters were allowed to vary freely. Fit uncertainties were obtained from the diagonal elements of the covariance matrix scaled by the square root of reduced chi-square ($1\sigma-$ uncertainty).

RESULTS AND DISCUSSION

Calibration and Estimation of Mn Valence of Manganese Oxides Using IPFY XAS Spectra. Soft IPFY XAS spectra at the Mn $L_{3,2}$-edge of powder Mn oxides were used to estimate the Mn valence as they were less susceptible to saturation effects than the PFY (Figure S5) and more reliably calibrated with common reference materials as compared to the total electron yield (TEY; Figure S5C), both of which were used in previous *ex situ* work.[43−46,61,82] These advantages of the IPFY resulted in the greatest sensitivity for Mn valence among the investigated methods. Figure 1A compares the IPFY spectra at the Mn $L_{3,2}$-edges of select phase-pure Mn oxide powders (Figure S12) with rocksalt, spinel, layered birnessite, and rutile structures (Figure 1B). These oxides have Mn valence in the range from 2+ to 4+ (Figure 1C). With increasing Mn valence, the centers of gravity of the Mn L_3-edges were found to linearly shift to higher energies. Of significance is that spinels of different Mn valence (i.e., $Mn^{2.7+}{}_3O_4$ and $LiMn^{3.5+}{}_2O_4$) have considerably different Mn L_3-edges, while spinel $LiMn^{3.5+}{}_2O_4$ and layered δ-$K_xMn^{3.5+}O_{2-y}{\cdot}zH_2O$ with comparable valence also exhibit comparable spectra. A Mn oxide film was electrodeposited by reduction of $KMnO_4$ at 1.33 V vs RHE. Its Mn L_3-spectrum of was found to have a sharp feature at ~642 eV and a broad peak at ~645 eV, which resembles those of spinel $LiMn^{3.5+}{}_2O_4$ and layered δ-$K_xMn^{3.5+}O_{2-y}{\cdot}zH_2O$ (Figure 1A) but differs from those of rocksalt MnO (octahedral Mn^{2+} with peaks at ~640 and ~641 eV) and spinel Mn_3O_4 (tetrahedral Mn^{2+} and octahedral Mn^{3+} with a peak at ~641 eV). On the basis of XRD performed on thicker films,[72] we assigned the electrodeposited film to δ-$K_xMn^{3.5+}O_{2-y}{\cdot}zH_2O$ (Figure S2). Using the linear correlation between the nominal Mn valence and the center of gravity of the Mn L_3-edges (Figure 1C), the electrodeposited film was found to have a valence of $Mn^{3.4+}$ after flushing the XAS cell and exchange of the $KMnO_4$ solution for O_2-saturated 0.1 M KOH (Figure S3). The calculated Mn valence of our film ($Mn^{3.4+}$) is lower than that of Mn oxides electrodeposited potentiostatically from solutions of 0.5 mM Mn chloride and 0.1 M methylphosphate at 0.58 V vs NHE ($Mn^{3.7+}$)[83] and at 1.05 V vs NHE ($Mn^{4.0+}$)[60] but higher than those electrodeposited by the same method at 0.85 V vs NHE ($Mn^{2.8+}$).[51] The latter's Mn valence is unusually low, and the authors discuss that their sample was reduced by X-ray irradiation. Our films were intermediate to those made by cycling (i) between 0.0 and 0.6 V vs Ag/AgCl at 20 mV/s and 900 rpm in Mn acetate and Na sulfate of 0.1 M each ($Mn^{3.1+}$)[43] and (ii) between +2.15 and 0.75 V vs NHE at 100 mV/s without rotation or stirring in 0.5 mM Mn acetate ($Mn^{3.8+}$).[15]

The O K-pre-edge accesses the density of Mn states through hybridization with oxygen states. In a completely ionic description of the Mn−O bond, all p-orbitals would be filled; thus, no X-ray absorption signal could be expected. Yet in a covalent description of the Mn−O bond, electrons are shared between Mn and O by hybridization of molecular orbitals. Thus, the background-subtracted area under the O K-pre-edge is a measure of the density of empty states on the Mn ion and the Mn−O hybridization of empty states.[84,85] Further in-depth discussion may be found in ref 84. The Mn valence is a measure

DOI: 10.1021/acs.jpcc.7b05592
J. Phys. Chem. C 2017, 121, 17682−17692

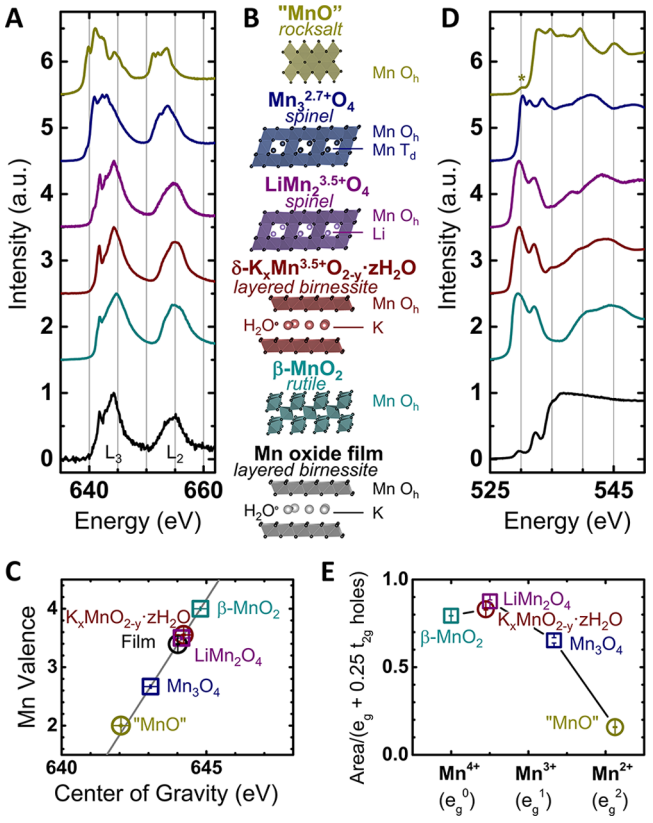

Figure 1. X-ray absorption spectroscopy at the (A) Mn $L_{3,2}$-edges of MnO, $Mn^{2.7+}{}_3O_4$, $LiMn^{3.5+}{}_2O_4$, δ-$K_xMn^{3.5+}O_{2-y}{\cdot}zH_2O$, and β-$Mn^{4+}O_2$ reference powders (Table S1) compared to those of Mn oxide electrodeposited on Au|CrO_x|Si_3N_4 and recorded in O_2-saturated 0.1 M KOH under flow. (B) Crystal structures of the measured oxides. (C) Mn valence obtained by calibration to the center of gravity of the Mn L_3-edge of reference Mn oxides (squares) and test references not used in the calibration (circles). Circles additionally show the fit uncertainty propagated from the calibration curve of the Mn valence (gray line) (D) O K-edges of all samples. (E) Estimation of the Mn–O hybridization according to Suntivich et al.[84] using the normalized O K-pre-edge area integrated between 529 and 532 eV. The pre-edge of the electrodeposited film is drastically reduced by 0.1 M KOH and can thus not be compared directly to the dry reference samples. O K-spectra were recorded in partial fluorescence yield and Mn $L_{3,2}$-spectra in inverse partial fluorescence yield. The maximum of each spectrum in panels A and D was normalized to unity and then offset. An asterisk indicates a Mn^{3+} impurity in the MnO spectrum (Figure S5D). Errors indicate the standard deviation of 3–10 spots on the samples (Tables S3 and S4).

of the empty states and increasing Mn valence is associated with a pronounced increase in the PFY O K-pre-edge features below 532 eV (Figure 1D,E). The shape and onset of the O K-pre-edges were found to drastically differ when going from MnO and Mn_3O_4 to $LiMn_2O_4$, while changes are subtler among $LiMn_2O_4$, $K_xMnO_{2-y}{\cdot}zH_2O$, and β-MnO_2. This is consistent with the trends observed at the Mn $L_{3,2}$-edges (Figure 1A).

Trends in hybridization of the references were obtained from the O K-pre-edge. The angular overlap of empty Mn 3d states with O 2p states depends on the orbital symmetry, where t_{2g} states contribute about 4 times less to the spectral intensity as compared to those with e_g symmetry.[84] Therefore, the contribution of the Mn states to the area under the pre-edge is removed by division of (h_{e_g} + 1/4 $h_{t_{2g}}$), where h_{eg} are the number of holes with e_g symmetry and $h_{t_{2g}}$ is the number of those with t_{2g} symmetry. As the large exchange energy mandates high spin, there are 3 holes with t_{2g} symmetry for all investigated oxides, and the number of e_g holes equals the Mn valence that was determined experimentally from the calibration curve in Figure 1C. The remaining area under the pre-edge is thus proportional to the hybridization of empty states, which we assume to be equal to the hybridization of filled states (i.e., covalence).[84] O K-pre-edges normalized by this established method[84] show increasing Mn–O hybridization with greater Mn valence (Figure 1E) for integration of the pre-edge intensities between 529 and 532 eV (arbitrarily defined). Mn–O hybridization in $LiMn_2O_4$, $K_xMnO_{2-y}{\cdot}zH_2O$, and β-MnO_2 is mostly due to Mn 3d orbitals because of the orbital energies of Mn^{3+} ($e_g^1t_{2g}^3$) and Mn^{4+} ($e_g^0t_{2g}^3$).[61,86] It should be noted that integration over the entire pre-edge of the O K-edge in Figure S9F includes the hybridization changes from unoccupied Mn 4s and Mn 4p orbitals (a_{1g} and t_{1u} of Mn^{2+}) in addition to those from unoccupied Mn 3d orbitals (e_g and t_{2g} of Mn^{3+} and Mn^{4+}). Thus, the entire pre-edge is not a suitable measurement of Mn–O hybridization because the orbital contributions change among the Mn oxides. The O K-edge spectrum of the electrodeposited film in O_2-saturated 0.1 M KOH was dominated by the signal of the aqueous electrolyte and the contribution of the Mn oxide to the total O K-signal was small (Figure 1D).

***In Situ* IPFY XAS at the Mn $L_{3,2}$-Edge and PFY XAS at the O K-Edge of Electrodeposited δ-$K_xMn^{3.5+}O_{2-y}{\cdot}zH_2O$ films.** Noticeable changes were found at different applied potentials in the IPFY XAS spectra of the Mn $L_{3,2}$-edges collected *in situ* on the electrodeposited film in a three-electrode cell, as shown in Figure 2A. At 1.65 V (steps 10a and 18a) and 1.50 V vs RHE (step 17a), the spectra strongly resembled that of the δ-$K_xMn^{3.5+}O_{2-y}{\cdot}zH_2O$ reference, while at 0.80 V (steps 13a and 15a) and 0.50 V vs RHE (step 14a), the spectra compared well with that of the $Mn^{2.7+}{}_3O_4$ reference that contains tetrahedral Mn^{2+}. The changes in the Mn valence of the electrodeposited films at different applied potentials were quantified using the calibration curve in Figure 1C. Using the spectra in Figure 2A (steps 10a–18a in Table S2), the valence was initially $Mn^{3.1+}$ at 1.65 V vs RHE, then gradually decreased with reducing potential to $Mn^{2.5+}$ at 0.50 V vs RHE (step 15a), and finally gradually increased with greater potential to $Mn^{3.3+}$ at 1.65 V vs RHE (step 18a). The film was reduced below an average valence of 3+ below the onset potential of ORR (~0.9 V vs RHE) and oxidized above an average valence of 3+ above the onset potential of OER (~1.6 V vs RHE). Therefore, our data support the investigated Mn oxide containing tetrahedral Mn^{2+} during ORR conditions and Mn^{4+} during OER conditions in addition to Mn^{3+}.

A hysteresis in the Mn valence associated with stepping the voltages down and up was noted in Figure 2B, which suggests that oxidation kinetics of the film are slower than the reduction kinetics. This hypothesis is supported by the observation that only the features of the δ-$K_xMn^{3.5+}O_{2-y}{\cdot}zH_2O$ reference were noted at OCV (step 7a), while all measurements after reduction at 0.80 V vs RHE (step 8a) retained a shoulder at 641.1 eV characteristic to Mn_3O_4. A similar hysteresis in the Mn valence changes is reported for electrodeposited Mn oxide between 0.7 and 1.9 V vs RHE in 0.1 M KPi[51] and for nanocrystalline hydrous Mn oxides between 0.65 and 1.65 V vs RHE in 2 M KCl,[59] where it has been attributed to poor electronic and ionic conductivity of Mn_3O_4 formed at low potentials. The hysteresis of the Mn valence affects the measured current densities

DOI: 10.1021/acs.jpcc.7b05592
J. Phys. Chem. C 2017, 121, 17682–17692

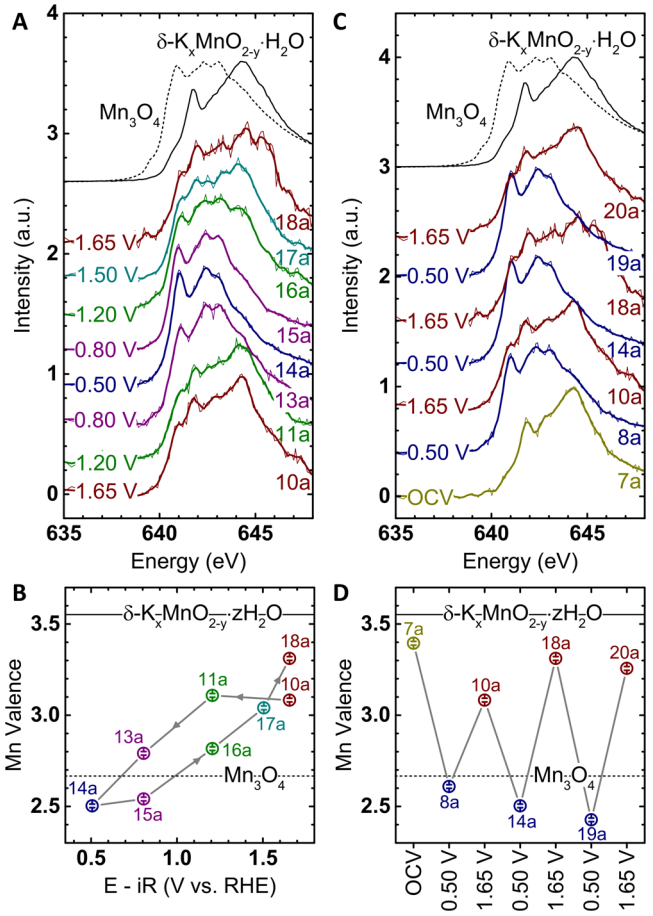

Figure 2. X-ray absorption spectroscopy of the electrodeposited film at the Mn $L_{3,2}$-edges recorded in inverse partial fluorescence mode using the three-electrode XAS cell with an Au|CrO_x|Si_3N_4 window while flowing O_2-saturated 0.1 M KOH. (A) Waterfall plot of the spectra during cycling from 1.65 V via 0.50 to 1.65 V vs RHE. (B) Trends of the Mn valence during cycling. (C) Waterfall plot of the spectra during alternating reduction (0.50 V vs RHE) and oxidation (1.65 V vs RHE) steps. (D) Trends of the Mn valence during alternating oxidation/reduction steps. Thick lines were smoothed by a second-order spline filter[87] using an 8 pt window. Powderous references of Mn_3O_4 (short dashed line) and δ-$K_xMnO_{2-y}\cdot zH_2O$ (solid line) are also included. All Mn valences were obtained using the calibration curve in Figure 1C, and error bars were propagated from the fit uncertainty of the calibration curve. The step number in Table S2 is also shown in each panel.

(Figure S13C), which suggests correlation with electrocatalysis. However, further *in situ*/*operando* experiments are required to clearly prove a catalytic role of the observed changes in Mn valence.

Partial reversibility of spectral changes was further demonstrated by repeating experiments between 0.50 V (ORR) and 1.65 V vs RHE (OER) three times (Figure 2C), where spectra at 0.5 V vs RHE resembled $Mn^{2.7+}{}_3O_4$ and spectra at 1.65 V vs RHE resembled that of δ-$K_xMn^{3.5+}O_{2-y}\cdot zH_2O$. Comparable Mn valence was obtained at the same applied potentials in these three repeats, as shown in Figure 2D, where the average valence during ORR was $Mn^{2.5+}$ and the average valence during OER was $Mn^{3.2+}$.

We further fit all spectra using those from powders of $Mn^{2.7+}{}_3O_4$ and δ-$K_xMn^{3.5+}O_{2-y}\cdot zH_2O$ to quantify the similarity to these standards and support the assignments above (Figure S8; further details are given in Experimental Section). In support of our previous discussion, the initial measurement at OCV (step 7a) showed (100 ± 2)% δ-$K_xMn^{3.5+}O_{2-y}\cdot zH_2O$ character, while reduction at 0.8 V vs RHE resulted in up to (99 ± 4)% $Mn^{2.7+}{}_3O_4$ character (step 14a) with an average of (87 ± 2)%, and oxidation at 1.65 V vs RHE was limited to (76 ± 2)% δ-$K_xMn^{3.5+}O_{2-y}\cdot zH_2O$ character (step 20) with an average of (71 ± 1)% (Figure S8). The excellent agreement with the Mn_3O_4 standard also corroborates Mn^{2+} having tetrahedral coordination in the investigated voltage range. The two most common analyses of soft XAS, calibration of the Mn valence and fitting standards; thus, both support partial reversibility of the Mn redox as well as tetrahedral Mn^{2+} at ORR conditions and Mn^{4+} at OER conditions.

In situ O K-edge PFY XAS spectra revealed partially reversible changes in the pre-edge with applied voltage (Figure 3). The O K-pre-edges were found to include a peak labeled (i) near 529.7 eV, which can be attributed mainly to δ-

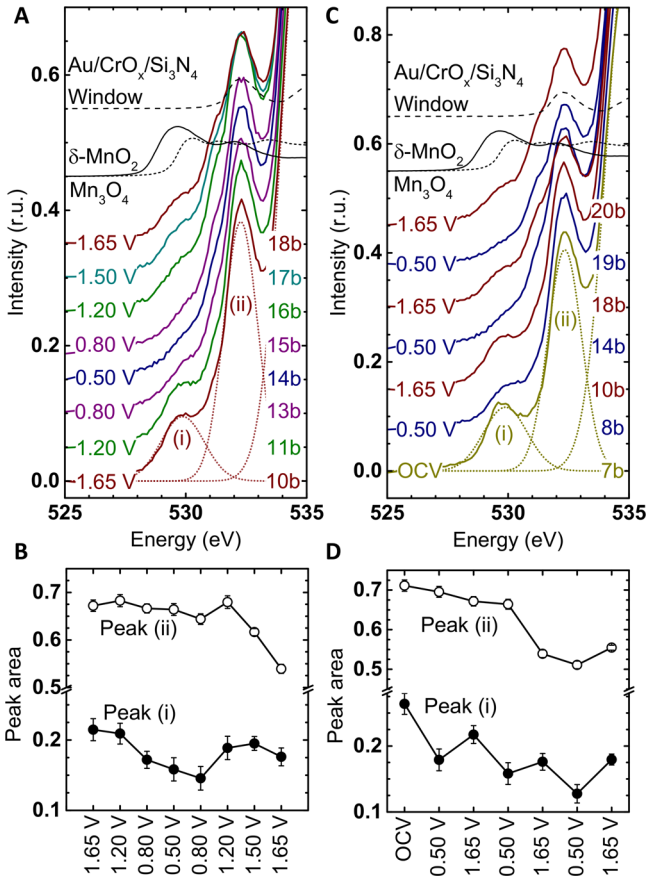

Figure 3. X-ray absorption spectroscopy of the electrodeposited film at the O K-edge recorded in partial fluorescence mode using the three-electrode XAS cell with an Au|CrO_x|Si_3N_4 window while flowing O_2-saturated 0.1 M KOH. (A) Waterfall plots of the O K-edge and (B) areas under peaks (i) and (ii) during cycling from 1.65 V via 0.50–1.65 V vs RHE. (C) Waterfall plots of the O K-edge and (D) areas under peaks (i) and (ii) during alternating reduction (0.50 V vs RHE) and oxidation (1.65 V vs RHE) steps. The voltages and step numbers in Table S2 are shown near each spectrum. Dotted lines show exemplary fits of peak (i) and peak (ii), further fits are in Figures S10 and S11. Reference spectra of Mn_3O_4 (short dashed line) and δ-$K_xMnO_{2-y}\cdot zH_2O$ (solid line) powders and a clean Au|CrO_x|Si_3N_4 window (long dashed line) are also included. Error bars indicate the fit uncertainty.

DOI: 10.1021/acs.jpcc.7b05592
J. Phys. Chem. C 2017, 121, 17682–17692

$K_xMn^{3.5+}O_{2-y}\cdot zH_2O$ with a minor contribution from $Mn^{2.7+}{}_3O_4$ at the high-energy side of the peak (Figure 3A) and a peak labeled (ii) at 532.3 eV already present in the Au|CrO_x|Si_3N_4 window with a strong background from both δ-$K_xMn^{3.5+}O_{2-y}\cdot zH_2O$ and $Mn^{2.7+}{}_3O_4$ (Figure 3A). The spectra were further analyzed by fitting Gaussians to these two peaks and a shoulder in the O K-edge as the background (Figures S10; further details are given in Experimental Section). The area under peak (i) decreased with applied voltage to a minimum at 0.80 V vs RHE (step 15b), after which it increased again (Figure 3B). In contrast, the area under peak (ii) remained relatively constant and then dropped steeply after step 16b. An identical analysis was performed for alternating oxidation at 1.65 V vs RHE and reduction at 0.50 V vs RHE (Figures 3C and S11), where again only the area under peak (i) followed the voltage but on a background of overall reducing peak area (Figure 3D). This suggests that peak (i) correlates with electronic properties of the electrodeposited film, while the diverging trend of peak (ii) suggests that it correlates with the degradation of the Au|CrO_x|Si_3N_4 window.

The ratio of the areas of peaks (i) to (ii) was employed to remove the influence of film loss due to degradation of the window material (Figure 4A). The resulting trend with voltage strongly resembles that of the Mn valence (Figure 4A) obtained from analysis of the Mn L_3-edge that is based on the experimental calibration in Figure 1C. Similarity among the trends in the O K-and Mn-L edge is expected as the metal d-band and oxygen p-band increase their overlap with higher valence in perovskites ABO_3 (B = Mn[45] and Ni[84]), which can serve as references for the electrodeposited film as the relevant metal 3d states are well separated from hybridization with other elements (e.g., A = Ca or Pr).[45,88] Highly similar trends between the peak area ratio and Mn valence were also observed for alternating reduction at 0.50 V vs RHE and oxidation at 1.65 V vs RHE (Figure 4B). Analysis of all recorded O K-pre-edges demonstrates clearly that the peak ratio scales linearly with the experimental Mn valence based on the L_3-edge (Figure 4C). Therefore, the presented analysis could be used to determine the metal valence state by *in situ* analysis of the O K-pre-edge if a suitable calibration was performed.

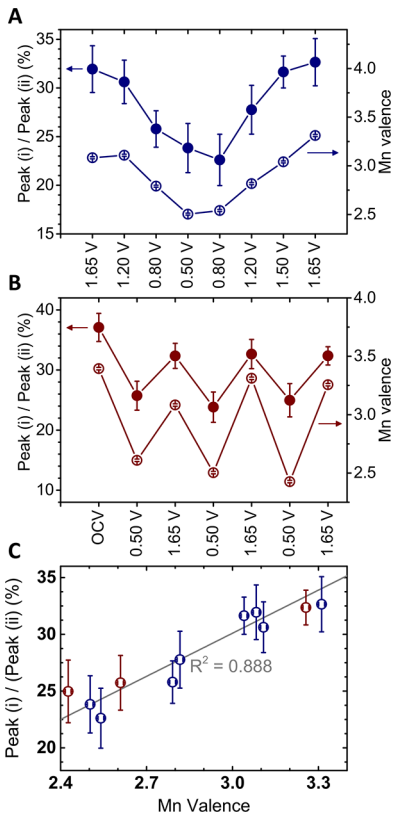

Figure 4. Trends of the area ratio (solid circles) of peak (i) to peak (ii) in Figure 3A,B (A) for cycling from 1.65 V vs RHE to 0.50 V vs RHE with intermediate voltages and back; as well as (B) for alternating reduction at 0.50 V vs RHE and oxidation at 1.65 V vs RHE. For comparison, the Mn valence (open circles) obtained from the calibration data in Figure 1C of the main text is also shown. (C) Linear correlation between the area ratios of peak (i) and peak (ii) in panels A and B with the Mn valence obtained from the calibration data in Figure 1C of the main text. Error bars were obtained by propagating the uncertainties of the fitted amplitudes of peaks (i) and (ii) as well as the uncertainties of the Mn valence calibration curve.

The pre-edge of the oxygen K-edge data is sensitive to both valence and hybridization as we discussed above for powder reference compounds in Figure 1. Having established the sensitivity of the *in situ* O K-data on Mn valence, we now analyze the hybridization, for which the peak ratios of the areas of peaks (i) and (ii) were further normalized by the weighted number of holes on the Mn cation (e_g holes +1/4t_{2g} holes)[84] obtained from the experimentally determined Mn valence. To emphasize relative changes, we divided by scan 10b (1.65 V) for decreasing voltage (Figure S14A), by scan 14b (0.50 V) for increasing voltage (Figure S14A), and by scan 7b (OCV) for alternating between 0.50 and 1.65 V vs RHE (Figure S14B). This normalized peak ratio decreased for reduction from $Mn^{3.1+}$ to $Mn^{2.5+}$ when decreasing the voltage from 1.65 to 0.50 V vs RHE and increased for oxidation from $Mn^{2.5+}$ to $Mn^{3.0+}$ (Figure S14A), but the obtained changes are not significant within the uncertainty of the ratios.

The *in situ* trends are qualitatively consistent with the *ex situ* trends of the reference samples in Figure 1E, where the hybridization decreased from the $Mn^{2.7+}{}_3O_4$ reference to the δ-$K_xMn^{3.5+}O_{2-y}\cdot zH_2O$ and $LiMn^{3.5+}{}_2O_4$ references. The spectrum of β-$Mn^{4+}O_2$ ($e_g{}^0$) showed a lower hybridization as compared to that of the $Mn^{3.5+}$ ($e_g{}^{0.5}$) references, which might explain the lower hybridization of the electrodeposited film with $Mn^{3.4+}$ ($e_g{}^{0.6}$) valence as compared to the $Mn^{3.0+}$ ($e_g{}^1$) valence when the e_g orbital is emptied. The reduction of the hybridization above Mn^{3+} ($e_g{}^1$) can also be seen qualitatively for alternating reduction at 0.50 V vs RHE and oxidation at 1.65 V vs RHE (Figure S14B), where the hybridization decreases for reduction and increases for oxidation, albeit not significantly within the uncertainty of the ratios. Additionally, the difference in hybridization qualitatively decreases with the difference in Mn valence (Figure S14B). In summary, analysis of the O K-pre-edge area shows qualitative trends of changes in Mn−O hybridization during *in situ* experiments, where an e_g occupancy near one likely corresponds to the highest hybridization.

In this report, we have analyzed changes of the Mn valence with applied voltage during *in situ* Mn $L_{3,2}$-and O K-edge XAS. Furthermore, we analyzed changes in the Mn−O hybridization of an electrodeposited Mn oxide for the first time using *in situ* O K-edge XAS. We found a mixed $Mn^{3+/4+}$ valence above applied potentials of 1.20 V vs RHE (i.e., clearly before the onset of the OER). This is in agreement with previous *in situ* studies on electrodeposited Mn oxides at the Mn K-[12,18,50,59] and Mn $L_{3,2}$-edges[51,60] in various electrolytes (0.1 M KOH,[18] 0.1 M KPi,[12,51,60] 0.1 M $NaSO_4$,[50] and 2 M KCl[59]). In our *in*

DOI: 10.1021/acs.jpcc.7b05592
J. Phys. Chem. C 2017, 121, 17682−17692

situ data, there is also clear evidence for 20% Mn^{4+} ions on average during oxygen evolution at 1.65 V vs RHE (Figure 4D), which disagrees with *ex situ* XPS studies of bixbyite Mn_2O_3.[21] The difference might be due to the drying procedure before XPS measurements or the higher crystallinity[43] of the material in the *ex situ* XPS study, which would hinder accumulation of holes and remove any excess charge during the XPS measurement where the sample is grounded. *Ex situ* XPS[16] and XAS[10,14,15,43] studies also clearly show a mixed $Mn^{3+/4+}$ valence after OER in 0.1 M KOH[14,43] and 0.1 M KPi[10,14−16] for less crystalline electrodeposited Mn oxides in agreement with our *in situ* XAS study.

The observation of tetrahedral Mn^{2+} during ORR in our *in situ* L-edge study is likewise in agreement with previous Mn K-edge reports where the spinel structure was identified by fitting the Mn K-edge spectra to references[47] and by EXAFS analysis.[18] In our data, the presence of tetrahedral Mn^{2+} can be directly seen as the emergence of a new peak, which greatly simplifies analysis. It is crucial to separate tetrahedral Mn^{2+} from the Mn valence at octahedral sites, which trend with ORR activity.[22] Our study demonstrates that this is possible by *in situ* experiments at the Mn $L_{3,2}$-edges, which allow faster acquisition as compared to EXAFS analysis at the Mn K-edge.

In situ analysis of the hybridization qualitatively supports the special role of single e_g occupancy for oxygen electrocatalysis. Understanding Mn−O hybridization is crucial for oxygen electrocatalysis because it relates to the adsorption of oxygen on the catalytic surface.[3] Similar *in situ* O K-edge studies have previously only been available for hematite (α-Fe_2O_3)[67,68] and electrodeposited Ni oxide.[69] We obtained this hybridization by analysis of the O K-pre-edge at various applied voltages, which was consistent with the trends identified based on valence from select *ex situ* references. The maximum of Mn−O hybridization is estimated for a valence close to Mn^{3+} with an e_g occupancy near unity, where the maximum activity for both OER and ORR was reported for perovskites[19,23,27] and spinels[22] based on *ex situ* analysis. Thus, the presented analyses at the Mn-L_3 and particularly O K-edges set the stage for correlations between Mn−O hybridization and catalytic activity toward testing known activity descriptors at catalytic conditions.

CONCLUSIONS

We probe changes in the Mn valence and Mn−O hybridization using IPFY XAS at the Mn $L_{3,2}$-edges and PFY XAS at the O K-edges of electrodeposited δ-$K_xMnO_{2-y}\cdot zH_2O$. Experiments are performed *in situ* in 0.1 M KOH solution as a function of voltages relevant to ORR and OER. IPFY Mn $L_{3,2}$-edges provide greater chemical sensitivity to Mn valence as compared to the conventional PFY detection, where the center of gravity of the Mn L_3-edge is established to correlate with the Mn valence using a number of reference Mn oxides. Using this calibration, the average Mn valence of electrodeposited δ-$K_xMnO_{2-y}\cdot zH_2O$ has been determined as a function of the applied voltage. The valence relevant to ORR is below Mn^{3+} and contains tetrahedral Mn^{2+}, while the valence relevant to OER is above Mn^{3+} and contains Mn^{4+} ions. Both are in accordance with previous *ex situ* and *in situ* studies on electrodeposited Mn oxides. Stepping back and forward between ORR and OER voltages is shown to be reversible, but there is hysteresis in the Mn valence, which can be attributed to slow oxidation kinetics of a Mn_3O_4-like phase with poor electronic conductivity as proposed by Chang et al.[59] *In situ* analysis of the O K-edge suggests that the Mn−O hybridization decreases for valences above and below Mn^{3+}. Combining this *in situ* insight with previous *ex situ* studies on perovskites[19,23,27] and spinels[22] fortifies the notion that having significant Mn^{3+} (i.e., about one e_g electron) is critical in catalyzing OER and ORR. Therefore, *in situ* experiments at both the metal L- and oxygen K-edges are a powerful approach for (1) identifying the active valences during electrocatalytic reactions and (2) the metal−oxygen hybridization of active catalysts.

ASSOCIATED CONTENT

Supporting Information

The Supporting Information is available free of charge on the ACS Publications website at DOI: 10.1021/acs.jpcc.7b05592.

TEM and SAED of δ-MnO_2; XAS of Mn^{2+} references; additional XAS spectra; XRD of Mn powders; electrochemical currents during XAS; Mn−-L_3 fit results; O K-fit results; physical data of Mn oxide powders; sequence of XAS measurements; analysis results of the Mn−L_3 and O K-edges; energy calibration of soft XAS in literature; calculation of absence of pH changes (PDF)

AUTHOR INFORMATION

Corresponding Authors

*E-mail: shaohorn@mit.edu.
*E-mail: mrisch@material.physik.uni-goettingen.de.

ORCID

Marcel Risch: 0000-0003-2820-7006
Kelsey A. Stoerzinger: 0000-0002-3431-8290
Zhichuan Xu: 0000-0001-7746-5920
Yang Shao-Horn: 0000-0001-8714-2121

Present Addresses

M.R.: Institute of Materials Physics, University of Goettingen, Göttingen, 37077, Germany.
S.Y.S.: Department of Chemistry, Faculty of Science, Cairo University, Giza 12613, Egypt.

Notes

The authors declare no competing financial interest.

ACKNOWLEDGMENTS

This work was supported in part by the Skoltech-MIT Center for Electrochemical Energy Storage and the Singapore-MIT Alliance for Research and Technology (SMART). This work made use of the MIT MRSEC Shared Experimental Facilities, supported by the National Science Foundation under award no. DMR-1419807. Research described in this paper was performed at the Canadian Light Source, which is supported by the Canadian Foundation for Innovation, Natural Sciences and Engineering Research Council of Canada, the University of Saskatchewan, the Government of Saskatchewan, Western Economic Diversification Canada, the National Research Council Canada, and the Canadian Institutes of Health Research. K.A.S. was supported in part by the National Science Foundation Graduate Research Fellowship under grant no. DGE-1122374. S.Y.S. is thankful for the support of a postdoctoral fellowship from the Natural Sciences and Engineering Research Council (NSERC) of Canada. We thank Dr. M. E. Abrishami for help with the XRD measurement of $LiMn_2O_4$.

DOI: 10.1021/acs.jpcc.7b05592
J. Phys. Chem. C 2017, 121, 17682−17692

REFERENCES

(1) Umena, Y.; Kawakami, K.; Shen, J.-R.; Kamiya, N. Crystal Structure of Oxygen-Evolving Photosystem II at a Resolution of 1.9 Å. *Nature* **2011**, *473* (7345), 55−60.

(2) Dau, H.; Limberg, C.; Reier, T.; Risch, M.; Roggan, S.; Strasser, P. The Mechanism of Water Oxidation: From Electrolysis via Homogeneous to Biological Catalysis. *ChemCatChem* **2010**, *2* (7), 724−761.

(3) Hong, W. T.; Risch, M.; Stoerzinger, K. A.; Grimaud, A. J. L.; Suntivich, J.; Shao-Horn, Y. Toward the Rational Design of Non-Precious Transition Metal Oxides for Oxygen Electrocatalysis. *Energy Environ. Sci.* **2015**, *8* (5), 1404−1427.

(4) Kurz, P. Biomimetic Water-Oxidation Catalysts: Manganese Oxides. *Top. Curr. Chem.* **2015**, *371*, 49−72.

(5) Najafpour, M. M.; Renger, G.; Hołyńska, M.; Moghaddam, A. N.; Aro, E.-M.; Carpentier, R.; Nishihara, H.; Eaton-Rye, J. J.; Shen, J.-R.; Allakhverdiev, S. I. Manganese Compounds as Water-Oxidizing Catalysts: From the Natural Water-Oxidizing Complex to Nanosized Manganese Oxide Structures. *Chem. Rev.* **2016**, *116* (5), 2886−2936.

(6) Barber, J.; Tran, P. D. From Natural to Artificial Photosynthesis. *J. R. Soc., Interface* **2013**, *10* (81), 20120984.

(7) Nocera, D. G. The Artificial Leaf. *Acc. Chem. Res.* **2012**, *45* (5), 767−776.

(8) Artero, V.; Chavarot-Kerlidou, M.; Fontecave, M. Splitting Water with Cobalt. *Angew. Chem., Int. Ed.* **2011**, *50* (32), 7238−7266.

(9) McConnell, I.; Li, G.; Brudvig, G. W. Energy Conversion in Natural and Artificial Photosynthesis. *Chem. Biol.* **2010**, *17* (5), 434−447.

(10) Zaharieva, I.; Najafpour, M. M.; Wiechen, M.; Haumann, M.; Kurz, P.; Dau, H. Synthetic Manganese−calcium Oxides Mimic the Water-Oxidizing Complex of Photosynthesis Functionally and Structurally. *Energy Environ. Sci.* **2011**, *4* (7), 2400−2408.

(11) Wiechen, M.; Zaharieva, I.; Kurz, P.; Dau, H. Layered Manganese Oxides for Water-Oxidation: Alkaline Earth Cations Influence Catalytic Activity in a Photosystem II-like Fashion. *Chem. Sci.* **2012**, *3* (7), 2330.

(12) Zaharieva, I.; González-Flores, D.; Asfari, B.; Pasquini, C.; Mohammadi, M. R.; Klingan, K.; Zizak, I.; Loos, S.; Chernev, P.; Dau, H. Water Oxidation Catalysis − Role of Redox and Structural Dynamics in Biological Photosynthesis and Inorganic Manganese Oxides. *Energy Environ. Sci.* **2016**, *9* (7), 2433−2443.

(13) Wiechen, M.; Berends, H.-M.; Kurz, P. Wateroxidation Catalysed by Manganese Compounds: From Complexes to "Biomimetic Rocks. *Dalt. Trans.* **2012**, *41* (1), 21−31.

(14) Bergmann, A.; Zaharieva, I.; Dau, H.; Strasser, P. Electrochemical Water Splitting by Layered and 3D Cross-Linked Manganese Oxides: Correlating Structural Motifs and Catalytic Activity. *Energy Environ. Sci.* **2013**, *6* (9), 2745.

(15) Zaharieva, I.; Chernev, P.; Risch, M.; Klingan, K.; Kohlhoff, M.; Fischer, A.; Dau, H. Electrosynthesis, Functional, and Structural Characterization of a Water-Oxidizing Manganese Oxide. *Energy Environ. Sci.* **2012**, *5* (5), 7081−7089.

(16) Huynh, M.; Shi, C.; Billinge, S. J. L.; Nocera, D. G. Nature of Activated Manganese Oxide for Oxygen Evolution. *J. Am. Chem. Soc.* **2015**, *137* (47), 14887−14904.

(17) Hocking, R. K.; Brimblecombe, R.; Chang, L.-Y.; Singh, A.; Cheah, M. H.; Glover, C.; Casey, W. H.; Spiccia, L. Water-Oxidation Catalysis by Manganese in a Geochemical-like Cycle. *Nat. Chem.* **2011**, *3* (6), 461−466.

(18) Gorlin, Y.; Lassalle-Kaiser, B.; Benck, J. D.; Gul, S.; Webb, S. M.; Yachandra, V. K.; Yano, J.; Jaramillo, T. F. In Situ X-Ray Absorption Spectroscopy Investigation of a Bifunctional Manganese Oxide Catalyst with High Activity for Electrochemical Water Oxidation and Oxygen Reduction. *J. Am. Chem. Soc.* **2013**, *135* (23), 8525−8534.

(19) Suntivich, J.; May, K. J.; Gasteiger, H. A.; Goodenough, J. B.; Shao-Horn, Y. A Perovskite Oxide Optimized for Oxygen Evolution Catalysis from Molecular Orbital Principles. *Science* **2011**, *334* (6061), 1383−1385.

(20) Scholz, J.; Risch, M.; Stoerzinger, K. A.; Wartner, G.; Shao-Horn, Y.; Jooss, C. Rotating Ring−Disk Electrode Study of Oxygen Evolution at a Perovskite Surface: Correlating Activity to Manganese Concentration. *J. Phys. Chem. C* **2016**, *120* (49), 27746−27756.

(21) Ramírez, A.; Hillebrand, P.; Stellmach, D.; May, M. M.; Bogdanoff, P.; Fiechter, S. Evaluation of MnO_X, Mn_2O_3, and Mn_3O_4 Electrodeposited Films for the Oxygen Evolution Reaction of Water. *J. Phys. Chem. C* **2014**, *118* (26), 14073−14081.

(22) Wei, C.; Feng, Z.; Scherer, G. G.; Barber, J.; Shao-Horn, Y.; Xu, Z. J. Cations in Octahedral Sites: A Descriptor for Oxygen Electrocatalysis on Transition-Metal Spinels. *Adv. Mater.* **2017**, *29*, 1606800.

(23) Stoerzinger, K. A.; Risch, M.; Han, B.; Shao-Horn, Y. Recent Insights into Manganese Oxides in Catalyzing Oxygen Reduction Kinetics. *ACS Catal.* **2015**, *5* (10), 6021−6031.

(24) Ge, X.; Sumboja, A.; Wuu, D.; An, T.; Li, B.; Goh, F. W. T.; Hor, T. S. A.; Zong, Y.; Liu, Z. Z. Oxygen Reduction in Alkaline Media: From Mechanisms to Recent Advances of Catalysts. *ACS Catal.* **2015**, *5* (8), 4643−4667.

(25) Nie, Y.; Li, L.; Wei, Z. Recent Advancements in Pt and Pt-Free Catalysts for Oxygen Reduction Reaction. *Chem. Soc. Rev.* **2015**, *44* (8), 2168−2201.

(26) Risch, M. Perovskite Electrocatalysts for the Oxygen Reduction Reaction in Alkaline Media. *Catal. 2017* **2017**, *7* (5), 154.

(27) Suntivich, J.; Gasteiger, H. A.; Yabuuchi, N.; Nakanishi, H.; Goodenough, J. B.; Shao-Horn, Y. Design Principles for Oxygen-Reduction Activity on Perovskite Oxide Catalysts for Fuel Cells and Metal-Air Batteries. *Nat. Chem.* **2011**, *3* (7), 546−550.

(28) Ryabova, A. S.; Napolskiy, F. S.; Poux, T.; Istomin, S. Y.; Bonnefont, A.; Antipin, D. M.; Baranchikov, A. Y.; Levin, E. E.; Abakumov, A. M.; Kéranguéven, G.; et al. Rationalizing the Influence of the Mn(IV)/Mn(III) Red-Ox Transition on the Electrocatalytic Activity of Manganese Oxides in the Oxygen Reduction Reaction. *Electrochim. Acta* **2016**, *187*, 161−172.

(29) Gorlin, Y.; Chung, C.-J.; Nordlund, D.; Clemens, B. M.; Jaramillo, T. F. Mn 3 O 4 Supported on Glassy Carbon: An Active Non-Precious Metal Catalyst for the Oxygen Reduction Reaction. *ACS Catal.* **2012**, *2* (12), 2687−2694.

(30) Cheng, F.; Shen, J.; Peng, B.; Pan, Y.; Tao, Z.; Chen, J. Rapid Room-Temperature Synthesis of Nanocrystalline Spinels as Oxygen Reduction and Evolution Electrocatalysts. *Nat. Chem.* **2011**, *3* (1), 79−84.

(31) Gorlin, Y.; Jaramillo, T. F. A Bifunctional Nonprecious Metal Catalyst for Oxygen Reduction and Water Oxidation. *J. Am. Chem. Soc.* **2010**, *132* (39), 13612−13614.

(32) Cheng, F.; Chen, J. Metal-Air Batteries: From Oxygen Reduction Electrochemistry to Cathode Catalysts. *Chem. Soc. Rev.* **2012**, *41* (6), 2172−2192.

(33) Cao, R.; Lee, J.-S.; Liu, M.; Cho, J. Recent Progress in Non-Precious Catalysts for Metal-Air Batteries. *Adv. Energy Mater.* **2012**, *2* (7), 816−829.

(34) Wei, W.; Cui, X.; Chen, W.; Ivey, D. G. Manganese Oxide-Based Materials as Electrochemical Supercapacitor Electrodes. *Chem. Soc. Rev.* **2011**, *40* (3), 1697−1721.

(35) Simon, P.; Gogotsi, Y. Materials for Electrochemical Capacitors. *Nat. Mater.* **2008**, *7* (11), 845−854.

(36) Ghodbane, O.; Pascal, J.-L.; Favier, F. Microstructural Effects on Charge-Storage Properties in MnO2-Based Electrochemical Supercapacitors. *ACS Appl. Mater. Interfaces* **2009**, *1* (5), 1130−1139.

(37) Goodenough, J. B.; Kim, Y. Challenges for Rechargeable Li Batteries. *Chem. Mater.* **2010**, *22* (3), 587−603.

(38) Thackeray, M. M. Manganese Oxides for Lithium Batteries. *Prog. Solid State Chem.* **1997**, *25* (1−2), 1−71.

(39) Winter, M.; Brodd, R. J. What Are Batteries, Fuel Cells, and Supercapacitors? *Chem. Rev.* **2004**, *104* (10), 4245−4270.

(40) Haas, O.; Ludwig, C.; Bergmann, U.; Singh, R. N.; Braun, A.; Graule, T. X-Ray Absorption Investigation of the Valence State and Electronic Structure of $La_{1-x}Ca_xCoO_{3-\delta}$ in Comparison with

DOI: 10.1021/acs.jpcc.7b05592
J. Phys. Chem. C 2017, 121, 17682−17692

$La_{1-x}Sr_xCoO_{3-\delta}$ and $La_{1-x}Sr_xFeO_{3-\delta}$. *J. Solid State Chem.* **2011**, *184* (12), 3163−3171.
(41) Celorrio, V.; Calvillo, L.; Dann, E.; Granozzi, G.; Aguadero, A.; Kramer, D.; Russell, A. E.; Fermín, D. J. Oxygen Reduction Reaction at $La_xCa_{1-x}MnO_3$ Nanostructures: Interplay between A-Site Segregation and B-Site Valency. *Catal. Sci. Technol.* **2016**, *6* (19), 7231−7238.
(42) van Oversteeg, C. H. M.; Doan, H. Q.; de Groot, F. M. F.; Cuk, T. In Situ X-Ray Absorption Spectroscopy of Transition Metal Based Water Oxidation Catalysts. *Chem. Soc. Rev.* **2017**, *46*, 102.
(43) Gorlin, Y.; Nordlund, D.; Jaramillo, T. F. The Role of Heat Treatment in Enhanced Activity of Manganese Oxides for the Oxygen Reduction and Evolution Reactions. *ECS Trans.* **2013**, *58* (1), 735−750.
(44) Khan, M.; Xiao, J.; Zhou, F.; Yablonskikh, M.; MacFarlane, D. R.; Spiccia, L.; Aziz, E. F. On the Origin of the Improvement of Electrodeposited MnOx Films in Water Oxidation Catalysis Induced by Heat Treatment. *ChemSusChem* **2015**, *8* (11), 1980−1985.
(45) Ebrahimizadeh Abrishami, M.; Risch, M.; Scholz, J.; Roddatis, V.; Osterthun, N.; Jooss, C. Oxygen Evolution at Manganite Perovskite Ruddlesden-Popper Type Particles: Trends of Activity on Structure, Valence and Covalence. *Materials* **2016**, *9* (12), 921.
(46) Stoerzinger, K. A.; Risch, M.; Suntivich, J.; Lü, W. M.; Zhou, J.; Biegalski, M. D.; Christen, H. M.; Ariando, T.; Venkatesan; Shao-Horn, Y. Ariando; et al. Oxygen Electrocatalysis on (001)-Oriented Manganese Perovskite Films: Mn Valency and Charge Transfer at the Nanoscale. *Energy Environ. Sci.* **2013**, *6* (5), 1582−1588.
(47) Lima, F. H. B.; Calegaro, M. L.; Ticianelli, E. A. Electrocatalytic Activity of Manganese Oxides Prepared by Thermal Decomposition for Oxygen Reduction. *Electrochim. Acta* **2007**, *52* (11), 3732−3738.
(48) Lima, F. H. B.; Calegaro, M. L.; Ticianelli, E. A. Investigations of the Catalytic Properties of Manganese Oxides for the Oxygen Reduction Reaction in Alkaline Media. *J. Electroanal. Chem.* **2006**, *590* (2), 152−160.
(49) Frydendal, R.; Seitz, L. C.; Sokaras, D.; Weng, T.-C.; Nordlund, D.; Chorkendorff, I.; Stephens, I. E. L.; Jaramillo, T. F. Operando Investigation of Au-MnOx Thin Films with Improved Activity for the Oxygen Evolution Reaction. *Electrochim. Acta* **2017**, *230*, 22−28.
(50) Yoshida, M.; Yomogida, T.; Mineo, T.; Nitta, K.; Kato, K.; Masuda, T.; Nitani, H.; Abe, H.; Takakusagi, S.; Uruga, T.; et al. In Situ Observation of Carrier Transfer in the Mn-oxide/Nb:SrTiO3 Photoelectrode by X-Ray Absorption Spectroscopy. *Chem. Commun.* **2013**, *49* (71), 7848.
(51) Schwanke, C.; Xi, L.; Lange, K. M. A Soft XAS Transmission Cell for Operando Studies. *J. Synchrotron Radiat.* **2016**, *23* (6), 1390−1394.
(52) Najafpour, M. M.; Madadkhani, S.; Tavahodi, M. Manganese Oxides Supported on Nano-Sized Metal Oxides as Water-Oxidizing Catalysts for Water-Splitting Systems: 3-Electrochemical Studies. *Int. J. Hydrogen Energy* **2017**, *42* (1), 60−67.
(53) Stoerzinger, K. A.; Lü, W.; Li, C.; Ariando; Venkatesan, T.; Shao-Horn, Y. Highly Active Epitaxial La(1-x)SrxMnO3 Surfaces for the Oxygen Reduction Reaction: Role of Charge Transfer. *J. Phys. Chem. Lett.* **2015**, *6* (8), 1435−1440.
(54) Jin, K.; Chu, A.; Park, J.; Jeong, D.; Jerng, S. E.; Sim, U.; Jeong, H.-Y.; Lee, C. W.; Park, Y.-S.; Yang, K. D.; et al. Partially Oxidized Sub-10 nm MnO Nanocrystals with High Activity for Water Oxidation Catalysis. *Sci. Rep.* **2015**, *5*, 10279.
(55) Jin, K.; Seo, H.; Hayashi, T.; Balamurugan, M.; Jeong, D.; Go, Y. K.; Hong, J. S.; Cho, K. H.; Kakizaki, H.; Bonnet-Mercier, N.; et al. Mechanistic Investigation of Water Oxidation Catalyzed by Uniform, Assembled MnO Nanoparticles. *J. Am. Chem. Soc.* **2017**, *139* (6), 2277−2285.
(56) Lassalle-Kaiser, B.; Gul, S.; Kern, J.; Yachandra, V. K.; Yano, J. In situ/Operando Studies of Electrocatalysts Using Hard X-Ray Spectroscopy. *J. Electron Spectrosc. Relat. Phenom.* **2017**, DOI: 10.1016/j.elspec.2017.05.001.
(57) Takashima, T.; Hashimoto, K.; Nakamura, R. Mechanisms of PH-Dependent Activity for Water Oxidation to Molecular Oxygen by MnO2 Electrocatalysts. *J. Am. Chem. Soc.* **2012**, *134* (3), 1519−1527.
(58) Takashima, T.; Hashimoto, K.; Nakamura, R. Inhibition of Charge Disproportionation of MnO2 Electrocatalysts for Efficient Water Oxidation under Neutral Conditions. *J. Am. Chem. Soc.* **2012**, *134* (44), 18153−18156.
(59) Chang, J.-K.; Lee, M.-T.; Tsai, W.-T. In Situ Mn K-Edge X-Ray Absorption Spectroscopic Studies of Anodically Deposited Manganese Oxide with Relevance to Supercapacitor Applications. *J. Power Sources* **2007**, *166* (2), 590−594.
(60) Xi, L.; Schwanke, C.; Xiao, J.; Abdi, F. F.; Zaharieva, I.; Lange, K. M. In Situ L-Edge XAS Study of a Manganese Oxide Water Oxidation Catalyst. *J. Phys. Chem. C* **2017**, *121*, 12003.
(61) Qiao, R.; Chin, T.; Harris, S. J.; Yan, S.; Yang, W. Spectroscopic Fingerprints of Valence and Spin States in Manganese Oxides and Fluorides. *Curr. Appl. Phys.* **2013**, *13* (3), 544−548.
(62) Groot, F. De. Multiplet Effects in X-Ray Spectroscopy. *Coord. Chem. Rev.* **2005**, *249* (1−2), 31−63.
(63) Krause, M. O.; Oliver, J. H. Natural Widths of Atomic *K* and *L* Levels, *K* α X-ray Lines and Several *K L L* Auger Lines. *J. Phys. Chem. Ref. Data* **1979**, *8* (2), 329−338.
(64) Koningsberger, D. C.; Mojet, B. L.; van Dorssen, G. E.; Ramaker, D. E. XAFS Spectroscopy; Fundamental Principles and Data Analysis. *Top. Catal.* **2000**, *10*, 143−155.
(65) Henke, B. L.; Gullikson, E. M.; Davis, J. C. X-Ray Interactions - Photoabsorption, Scattering, Transmission and Reflection at E = 50−30,000 eV, Z = 1−92. *At. Data Nucl. Data Tables* **1993**, *54* (2), 181−342.
(66) Risch, M.; Ringleb, F.; Kohlhoff, M.; Bogdanoff, P.; Chernev, P.; Zaharieva, I.; Dau, H. Water Oxidation by Amorphous Cobalt-Based Oxides: In Situ Tracking of Redox Transitions and Mode of Catalysis. *Energy Environ. Sci.* **2015**, *8*, 661−674.
(67) Braun, A.; Sivula, K.; Bora, D. K.; Zhu, J.; Zhang, L.; Grätzel, M.; Guo, J.; Constable, E. C. Direct Observation of Two Electron Holes in a Hematite Photoanode during Photoelectrochemical Water Splitting. *J. Phys. Chem. C* **2012**, *116* (32), 16870−16875.
(68) Bora, D. K.; Braun, A.; Erat, S.; Ariffin, A. K.; Löhnert, R.; Sivula, K.; Töpfer, J.; Grätzel, M.; Manzke, R.; Graule, T.; et al. Evolution of an Oxygen Near-Edge X-Ray Absorption Fine Structure Transition in the Upper Hubbard Band in α-Fe_2O_3 upon Electrochemical Oxidation. *J. Phys. Chem. C* **2011**, *115* (13), 5619−5625.
(69) Yoshida, M.; Mitsutomi, Y.; Mineo, T.; Nagasaka, M.; Yuzawa, H.; Kosugi, N.; Kondoh, H. Direct Observation of Active Nickel Oxide Cluster in Nickel−Borate Electrocatalyst for Water Oxidation by In Situ O K-Edge X-Ray Absorption Spectroscopy. *J. Phys. Chem. C* **2015**, *119* (33), 19279−19286.
(70) Achkar, A. J.; Regier, T. Z.; Wadati, H.; Kim, Y.-J.; Zhang, H.; Hawthorn, D. G. Bulk Sensitive X-Ray Absorption Spectroscopy Free of Self-Absorption Effects. *Phys. Rev. B: Condens. Matter Mater. Phys.* **2011**, *83* (8), 81106.
(71) Devaraj, S.; Munichandraiah, N. Effect of Crystallographic Structure of MnO2 on Its Electrochemical Capacitance Properties. *J. Phys. Chem. C* **2008**, *112* (11), 4406−4417.
(72) Nakayama, M.; Nishiyama, M.; Shamoto, M.; Tanimoto, T.; Tomono, K.; Inoue, R. Cathodic Synthesis of Birnessite-Type Layered Manganese Oxides for Electrocapacitive Catalysis. *J. Electrochem. Soc.* **2012**, *159* (8), A1176−A1182.
(73) Risch, M.; Stoerzinger, K. A.; Regier, T. Z.; Peak, D.; Sayed, S. Y.; Shao-Horn, Y. Reversibility of Ferri-/Ferrocyanide Redox during Operando Soft X-Ray Spectroscopy. *J. Phys. Chem. C* **2015**, *119* (33), 18903−18910.
(74) Gorlin, Y.; Jaramillo, T. F. Investigation of Surface Oxidation Processes on Manganese Oxide Electrocatalysts Using Electrochemical Methods and Ex Situ X-Ray Photoelectron Spectroscopy. *J. Electrochem. Soc.* **2012**, *159* (10), H782−H786.
(75) Regier, T.; Krochak, J.; Sham, T. K.; Hu, Y. F.; Thompson, J.; Blyth, R. I. R. Performance and Capabilities of the Canadian Dragon: The SGM Beamline at the Canadian Light Source. *Nucl. Instrum. Methods Phys. Res., Sect. A* **2007**, *582* (1), 93−95.
(76) Hitchcock, A. P.; Brion, C. E. K-Shell Excitation Spectra of CO, N2 and O2. *J. Electron Spectrosc. Relat. Phenom.* **1980**, *18* (1), 1−21.

DOI: 10.1021/acs.jpcc.7b05592
J. Phys. Chem. C 2017, 121, 17682−17692

(77) van Schooneveld, M. M.; DeBeer, S. A Close Look at Dose: Toward L-Edge XAS Spectral Uniformity, Dose Quantification and Prediction of Metal Ion Photoreduction. *J. Electron Spectrosc. Relat. Phenom.* **2015**, *198*, 31−56.
(78) Ravel, B.; Newville, M. ATHENA, ARTEMIS, HEPHAESTUS: Data Analysis for X-Ray Absorption Spectroscopy Using IFEFFIT. *J. Synchrotron Radiat.* **2005**, *12* (4), 537−541.
(79) de Groot, F. M. F. Dips and Peaks in Fluorescence Yield X-Ray Absorption Are due to State-Dependent Decay. *Nat. Chem.* **2012**, *4* (10), 766−7−8.
(80) Miedema, P. S.; Wernet, P.; Föhlisch, A. State-Dependent Fluorescence Yields through the Core-Valence Coulomb Exchange Parameter. *Phys. Rev. A: At., Mol., Opt. Phys.* **2014**, *89* (5), 52507.
(81) Green, R. J.; Peak, D.; Achkar, A. J.; Tse, J. S.; Moewes, A.; Hawthorn, D. G.; Regier, T. Z. Comment on `State-Dependent Electron Delocalization Dynamics at the Solute-Solvent Interface: Soft-X-Ray Absorption Spectroscopy and Ab Initio Calculations". *Phys. Rev. Lett.* **2014**, *112* (12), 129301.
(82) Gilbert, B.; Frazer, B. H.; Belz, A.; Conrad, P. G.; Nealson, K. H.; Haskel, D.; Lang, J. C.; Srajer, G.; De Stasio, G. Multiple Scattering Calculations of Bonding and X-Ray Absorption Spectroscopy of Manganese Oxides. *J. Phys. Chem. A* **2003**, *107* (16), 2839−2847.
(83) Huynh, M.; Bediako, D. K.; Liu, Y.; Nocera, D. G. Nucleation and Growth Mechanisms of an Electrodeposited Manganese Oxide Oxygen Evolution Catalyst. *J. Phys. Chem. C* **2014**, *118* (30), 17142−17152.
(84) Suntivich, J.; Hong, W. T.; Lee, Y.-L.; Rondinelli, J. M.; Yang, W.; Goodenough, J. B.; Dabrowski, B.; Freeland, J. W.; Shao-Horn, Y. Estimating Hybridization of Transition Metal and Oxygen States in Perovskites from O K -Edge X-Ray Absorption Spectroscopy. *J. Phys. Chem. C* **2014**, *118* (4), 1856−1863.
(85) de Groot, F. M. F.; Grioni, M.; Fuggle, J. C.; Ghijsen, J.; Sawatzky, G. A.; Petersen, H. Oxygen 1 S X-Ray-Absorption Edges of Transition-Metal Oxides. *Phys. Rev. B: Condens. Matter Mater. Phys.* **1989**, *40* (8), 5715−5723.
(86) Sherman, D. M. The Electronic Structures of Manganese Oxide Minerals. *Am. Mineral.* **1984**, *69* (7−8), 788−799.
(87) Savitzky, A.; Golay, M. J. E. Smoothing and Differentiation of Data by Simplified Least Squares Procedures. *Anal. Chem.* **1964**, *36* (8), 1627−1639.
(88) Sotoudeh, M.; Rajpurohit, S.; Blöchl, P.; Mierwaldt, D.; Norpoth, J.; Roddatis, V.; Mildner, S.; Kressdorf, B.; Ifland, B.; Jooss, C. Electronic Structure of $Pr_{1-x}Ca_xMnO_3$. *Phys. Rev. B: Condens. Matter Mater. Phys.* **2017**, *95*, 23515.

DOI: 10.1021/acs.jpcc.7b05592
J. Phys. Chem. C 2017, 121, 17682−17692